Premixed Flame-Assisted Spray Pyrolysis Synthesis of Lithium Manganese Oxide Particles

Hamid Iravani[1], Mohammad Hojjat[1*], Mohsen Gholami[1], Mohammad Reza Talaie [2], Seyedfoad Aghamiri[1]
[1]*Department of Chemical Engineering, Faculty of Engineering, University of Isfahan, Isfahan, IRAN*
[2]*Chemical Engineering Department, Faculty of Chemical, Oil and Gas Engineering, Shiraz University, Molasadra St., Shiraz, Iran*
** Corresponding author: Department of Chemical Engineering, Faculty of Engineering, University of Isfahan, Isfahan, Iran. Tel.: +98-3137937074, Fax: +98-3137934031*
Email Address: m.hojjat@eng.ui.ac.ir

Abstract
Production of $LiMn_2O_4$ from aqueous solutions containing $LiNO_3$ and $Mn(NO_3)_2{\cdot}4H_2O$ in a premixed flame-assisted spray pyrolysis reactor was investigated. The effect of air to fuel flow ratio and residence time on flame length, flame temperature, product crystallinity, mean particle diameter, and yield were investigated. The effect of fuel flow and the concentration of the reactant solution on the average particle size and yield were studied. According to the thermal gravimetry test, $LiNO_3$ decomposed to Li_2O at 700°C and $Mn(NO_3)_2$ decomposed to manganese oxides between 180°C to 500°C. Also, the mixture of reactants converted to $LiMn_2O_4$ at about 480°C. The XRD patterns revealed Mn_2O_3 as the main impurity. The average size of the crystals was in the range of 20 to 50 nm. The dynamic light scattering test showed that the maximum and the minimum mean particle sizes were 436 and 210 nm, respectively. The highest product separation efficiency was 30%. Further investigation is needed to identify and quantify loss mechanisms such as wall deposition and gas-phase nucleation leading to filter bypass. Future improvements could include optimizing reactor geometry, using cyclone separators more effectively, and modifying the flame configuration to reduce particle loss.

Keywords: Spray pyrolysis; Premixed flame; Lithium manganese oxide; Crystallinity, Mean particle sizes

Introduction

The most important methods of nanoparticle production are the ball mill process (solid-phase reaction) and chemical-wet processes, including sol-gel, coprecipitation, hydrothermal methods, and aerosol processes. However, the ball mill process and chemical-wet processes are multistage and discontinuous. In addition, it is not easy to control the properties of particles, such as size and shape. In addition, these methods are not commercially suitable for large-scale use [1-4]. The aerosol process is considered a bottom-up process with the scale-up capability to produce homogeneous nanostructures with a narrow size distribution [5]. Due to features such as high rate and low production time, relative simplicity, and low operation cost, this is an assuring and reliable process, especially for commercial production of nanoparticles [6]. The aerosol method produces millions of tons of nanoparticles (such as carbon black, titania pigments, silica, optical fibers, and complex oxides) annually [7, 8]. The flame method is a subset of the aerosol process. It is a single-stage, economical and continuous process on a laboratory and industrial scale in which feed (including reactants and solvents) is sprayed into the flame [9]. After the solvent evaporates, a rapid reaction takes place. The flame provides the energy needed for the reaction.

In spray pyrolysis, another subset of the aerosol process, droplets atomize and enter a hot environment. The heat source causes the solvent to evaporate from the droplets, leading to the precipitation and decomposition of the solutes, thereby producing product particles in the micron or sub-micron size range. Because each droplet acts as a micro-reactor, production in a spray pyrolysis reactor results in acceptable uniformity and high reproducibility. In other words, the vital difference between the two methods is the type of heat source used in the reactor. In the flame method, the size and shape of the particles can be well controlled due to the possibility of changing the flow rate of the inlet flows. This method is divided into two categories according to the state of the feed; A) vapor-fed aerosol synthesis; in this method, reactants are injected into the flame in the vapor phase and are mainly used to produce ceramic materials. This method is used industrially to produce fumed silica, alumina, and titania. However, due to the high cost of volatile reagents, a limited number of products are produced by this method, B) liquid-fed aerosol flame synthesis production of flame aerosol with liquid feed: Reagents are injected into the flame in the liquid phase. Due to non-volatile reagents (liquid phase), the latter is more efficient, and more diverse products can be synthesized [7, 10-12]. The liquid-fed aerosol flame synthesis includes flame spray pyrolysis (FSP) and flame-assisted spray pyrolysis (FASP). In the FSP method, the reactants are dissolved in an organic solvent (solvent with high combustion enthalpy), and a small flame is used to provide combustion. In the FASP method, the reactants are the aqueous solution (solvent with low combustion enthalpy), and a hydrogen or hydrocarbon auxiliary flame is used for combustion [13, 14]. FASP is commercially more cost-effective due to the possibility of using cheap reagents and solvents (water and ethanol) [14]. In other words, the important difference between the two methods is the type of solvent used in the reaction solution. In FASP, after thermal decomposition reactions, the particles are separated from the reactor by a filter. Due to the spraying of reactant particles, intermolecular collisions are very effective and increase the reaction rate. On the other hand, direct contact of the droplets with the flame, while increasing the thermal efficiency, prevents the droplets from merging into each other and producing large particles. These reactors are also categorized into diffused flame and premixed flame based on the type of flame. In premixed flames, due to the mixing of fuel and oxidizer and the possibility of adjusting the oxidant to fuel ratio, a complete combustion process is performed, which leads to reduced fuel consumption, better temperature control and energy savings [15]. Many attempts have been devoted to model particle formation mechanisms in the flame process [16-18]. There are two mechanisms of gas-to-particle conversion and droplet-to-particle conversion. In the vapor phase aerosol process, particle formation occurs only through the gas-to-particle conversion mechanism. However, the liquid phase aerosol method may involve both mechanisms [18]. The flame method has received much attention from researchers due to its ability to produce particles commercially. Compared to traditional methods like sol-gel and co-precipitation, flame-assisted spray pyrolysis offers a one-step, continuous, and scalable approach with better control over particle size and crystallinity. However, it may yield lower purity if not optimized, and the process involves higher thermal input. Despite these trade-offs, FASP remains highly attractive for industrial-scale nanoparticle production due to its simplicity and speed. Recent work [19, 20] has demonstrated advancements in nanoparticle synthesis using spray pyrolysis techniques, further underscoring the relevance of optimizing flame conditions for high-performance battery materials. Jang et al. [21] investigated the effect of the concentration of the reactant solution and the fuel and oxidant flow on the size of $LiCoO_2$ nanoparticles produced by flame-assisted spray pyrolysis. They reported that an increase in the reactant solution's concentration leads to an increase in particle size. In addition, they found that by an increase in

the fuel and oxidant flow rate, the flame temperature increases, and larger particles are produced. Ernst et al. [22] used Li-t-butoxide, Mn(III)-acetylacetonate and xylene as solvents to produce $LiMn_2O_4$ spinel by flame spray pyrolysis. They found that increasing the feed flow from 3 to 8 ml/min, decreasing the carrier gas flow from 6 to 3 l/min, and raising the concentration of reactants up to 1.8 M significantly influenced the particle characteristics. These changes led to an increase in particle size, which jumped from 7 to 22 nm. At the same time, the specific particle surface area decreased, dropping from 200 to 65 m^2/g. Aromaa et al. [23] produced TiO_2 nanoparticles by spray flame pyrolysis. They studied the effect of feed flow on the particle size and flame length and observed that with increasing the feed flow, the flame becomes longer and thicker, and the nanoparticle size decreases. Patey et al. [24] investigated the effect of reactant solution flow rate and the carrier gas flow rate on the size and crystallinity of $LiMn_2O_4$ nanoparticles produced by spray flame pyrolysis. The effect of fuel flow rate on the average size distribution of crystals in the production of $LiMn_2O_4$ particles by flame spray pyrolysis of the aqueous solution has been investigated by Yi et al. [25]. Choi et al. Studied the modified $LiMn_2O_4$ nanoparticles by FASP and the effect of the modifier Lithium boron oxide (Li_2O-$2B_2O_3$) on the particle and crystal size [26]. Saadatkhah et al. [2] produced $LiMn_2O_4$ particles from reactants $Mn(NO_3)_2{\cdot}4H_2O$, Li_2CO_3, $LiNO_3$, and $Mn(CH_3CO_2)_2{\cdot}4H_2O$, by FASP. They found that droplets evaporated more slowly on acetate and carbonate reactants due to higher decomposition temperatures than on the nitrate reactants, which caused the particles to shrink and wrinkle. However, in the case of the nitrate reactants, due to the low decomposition temperature, the droplets evaporate faster and porous particles are obtained. Abram et al. [16] investigated the effect of spray droplet size on the particle size of yttrium oxide (Y_2O_3) produced in an FSP reactor. They reported that if the droplets of the reactant solution were large and the flame temperature was low, the particles would be hollow and large. If the flame temperature were high, particles with a wide size distribution would be obtained. If the droplet size is small and the flame temperature is low, large particles are produced by the droplet-to-particle mechanism. If the flame temperature is high, tiny particles are produced by the gas-to-particle mechanism. The concentration of the reactant solution has an insignificant effect on the particle size if droplet sizes to be small and flame temperature is low. Aboulouard et al. [27] compared the photovoltaic performance of solar cells made of titanium oxide nanoparticles (TiO_2) synthesized by the FSP method with solar cells made of titanium oxide nanoparticles synthesized by the thermal gel method. Zhang et al. Produced $LiNi_{0.8}Co_{0.15}Al_{0.05}O_2$ (NCA) cathodic powders using FASP and spray dryer using glycerol solvent. The results showed that the particles produced by FASP were smaller in size and smoother surface [28]. Madero et al. [29] Proposed a low-temperature FSP to produce $Li_{1.2}Mn_{0.54}Ni_{0.13}Co_{0.13}O_2$. In this method, the solvent was a mixture of water and ethanol, which also acted as fuel. Investigating the effect of ethanol percentage in mixture with water on the electrochemical properties of particles showed that the best results are obtained in 25% by weight of ethanol.

Flame synthesis holds promise for producing catalysts with controlled structures. Minegishi et al. [30] have synthesized Pt/CeO_2 nanoparticles using FASP at varying flame temperatures and evaluated for CO oxidation. The catalysts exhibited a bimodal structure, with both large CeO_2 particles (~100 nm) and smaller ones (<10 nm) hosting highly dispersed Pt clusters. Higher flame temperatures improved the BET surface area, Pt dispersion, and catalytic performance, reducing the temperature for complete CO conversion from 513 K to 378 K. Additionally, FASP-synthesized catalysts showed superior thermal stability and performance compared to those prepared by conventional methods, highlighting the promise of FASP for advanced catalyst

development. Chen et al. [31] investigated Ni-doped nano-Fe/Ce oxygen carriers (OCs) synthesized via flame spray pyrolysis (FSP) for chemical looping dry reforming of methane (CL-DRM). Thermodynamic analysis shows that Fe_2O_3 is reduced to Fe_3O_4 and Fe during reactions with CH_4, while CO_2 reoxidizes Fe. Experimental results reveal that an OC with a Ni/Fe molar ratio of 2/98 achieves over 30% CH_4 conversion, 90% CO selectivity, and stable cyclic performance. The FSP process enhances Ni dispersion and forms stable NiCe and NiFe alloys, while the transformation of Fe oxides and CeO_2 into $CeFeO_3$ improves lattice oxygen availability and stability. These findings demonstrate the potential of FSP-synthesized OCs for efficient CL-DRM. This work highlights the importance of advanced synthesis techniques in developing high-performance oxygen carriers for sustainable energy applications. The irrational use of antibiotics has prompted the need for effective wastewater treatment methods. A recent study employed one-step FSP to synthesize $Bi_4Ti_3O_{12}/TiO_2$ heterostructures, forming a "Z-type" heterojunction that enhances charge separation and electron transfer [32]. This material achieved 99.7% tetracycline removal under simulated sunlight for 75 minutes at 1V, demonstrating excellent reusability and stability. Free radical trapping experiments highlighted the key role of hydroxyl radicals and holes in degradation. These results highlight the potential of FSP-synthesized heterostructures for efficient pollutant removal [32].

The study of scientific sources shows that one of the most crucial challenges related to particle production in the aerosol process, especially the flame method, is the lack of necessary and sufficient data for the design and industrialization of the reactor, with the aim of commercialization and economical production of the product. Another major bottleneck in this process is identifying particle formation mechanisms in the reactor to control and improve the final properties of the product. Reaction temperature, a saturation of the reactant solution and residence time of particles are other critical parameters in the production process and the mechanism of particle formation in the flame. Given the importance of using renewable energy sources in preventing global warming, the pivotal role of storing energy produced from renewable sources becomes clear. Rechargeable lithium-ion batteries are one of the best options for energy storage and an integral part of our daily lives. One of the main components of these batteries is the spinel of lithium manganese oxide ($LiMn_2O_4$). The entry and exit of ions into the spinel structure are possible without any change in the spinel's shape, crystallinity, and volume. The electrochemical performance of these particles is affected by the purity, crystallinity, and particle size. Therefore, for the commercial production of these particles, it is necessary to develop processes with two capabilities: good controlling the particle properties and scale-up. In this research, a flame-assisted spray pyrolysis reactor was fabricated and used to study the effect of various operational variables on the synthesis of lithium manganese spinel.

Materials and Methods

$LiNO_3$ and $Mn(NO_3)_2{\cdot}4H_2O$ (Scharlau, Spain) were used as reagents. City gas, the composition of which is given in

Figure 1: Schematic of flame-assisted spray pyrolysis reactor setup

1- Ultrasonic spraying system, 2-Quartz cylindrical reactor with a length of 600mm and a diameter of 80mm, 3-Torch with triple inlet, 4-Product collection system including filter, 5-Fuel (city gas), 6 -Carrier gas (air), 7-Oxidizing agent (air)

Figure 2: Schematic of reactant solution spray system

1-Ultrasonic misting, 2- Carrier gas (air), 3- Spray nozzle with an inner diameter of 4 mm and an outer diameter of 20 mm

Figure 3: Schematic of the particle collection system

1-Gas flow inlet, 2- Metal filter with a diameter of 60 nm, 3- Fiberglass filter with a diameter of 60 nm, 4- Filter holder with an inner diameter of 60 nm and an outer diameter of 100 nm, 5- Gas flow output

Figure 4: TGA diagrams for pure $LiNO_3$ and $Mn(NO_3)_2.4H_2O$ Figure 5: TGA diagram of the stoichiometric mixture of $LiNO_3$ and $Mn(NO_3)_2.4H_2O$

Figure 6: Diffraction pattern of samples in different ratios of air to fuel at a concentration of 2M

Figure 7: Diffraction pattern of samples in different ratios of air-to-fuel at a concentration of 1.1 M

Figure 8: Scattering pattern of samples in different ratios of air-to-fuel at a concentration of 0.2 M

Table 1: City gas Composition

Table 2: Levels and variables selected for experiment design

Table 3: Experimental design recommended by the response surface methodology

Table 4: Flame temperature and height for different ratios of airflow to fuel flow

Table 5: Product production efficiency for the tests in Table 2

Table 6: Results of variance test for yield

Table 7: Results of variance test for average particle size

Table **8** was used as fuel, air as the oxidizer and carrier gas, and deionized water as solvent.

Figure 1 shows the schematic diagram of the experimental setup used in this research. First, the reactant solution is converted into ultra-fine droplets by ultrasonic misting. Then, airflow, the carrier gas, injects droplets into the flame through a spray nozzle. The flow meters measure the inlet currents to the reactor, including fuel, air (oxidizing gas and carrier gas). The test procedure is summarized below. By dissolving $LiNO_3$ and $Mn(NO_3)_2.4H_2O$ (with a molar ratio of lithium to the manganese of 1:2) in ion-free water, a reactive solution of the desired concentration is prepared. The solution is reduced to very fine droplets by ultrasonic misting and is sprayed into the initial part of the flame by an air stream (carrier gas) with a constant flow of 10 ml/min through the spray nozzle (Figure). A solenoid valve cuts off the fuel flow when the flame is extinguished. The filters installed outside the reactor in the gas flow path, Figure , collect the generated particles. A cyclone is placed in the gas flow path after the filter to increase yield. Further investigation is needed to identify and quantify loss mechanisms such as wall deposition and gas-phase nucleation leading to filter bypass. Future improvements could include optimizing reactor geometry, using cyclone separators more effectively, and modifying the flame configuration to reduce particle loss.
The hot gas stream leaving the reactor is dehumidified by passing through the cold-water chamber and then passing through the silica gel chamber and entering the vacuum pump. The particles are washed three times with ethanol and three times with distilled water and dried in a dryer for 24 hours at 80°C. The dried particles are put in a furnace for 5 hours at a temperature of 600°C at a heating rate of 2°C/min to increase the crystallinity of $LiMn_2O_4$ crystals and remove impurities.
One limitation of using nitrate-based precursors in the FASP method is the generation of nitrogen oxides (NO_X), such as NO and NO_2, during pyrolysis. These emissions can pose environmental and operational challenges, potentially affecting reaction stability and product purity. Future work may explore the use of alternative, more environmentally benign precursors, such as acetates or carbonates, which decompose at higher temperatures and produce fewer gaseous byproducts. Incorporating a post-flame gas scrubbing or catalytic reduction step can also help mitigate NO_X emissions in large-scale applications.

Design of experiments

The experiments were designed using the response level method and the central composite design (CCD) mode using the Design-Expert software. The air flow rate to fuel flow rate ratio and the concentration of the reactant solution were selected as independent parameters. In these experiments, the responses were average particle size and product separation efficiency. Preliminary experiments showed the flame was stable at an air flow rate of 1 cubic meter per hour and fuel flow rates between 80 and 150 liters per hour. Therefore, air flow rate to fuel flow rate ratios were selected at three levels of 6.5, 9.5 and 12.5. Furthermore, the levels for the concentration of the reactant solution were selected at 0.2, 1.1, and 2 M. Table **9** shows the variables and levels selected in the experiment design. According to the selected parameters and levels, the response level method offered ten experiments according to Table **10**, including eight experiments related to factorial levels and two experiments related to the central point.

Characterization

An X-ray diffraction device (model D8-ADVANCE, Bruker Germany) was used to study the structure and identify the crystalline phases in the produced particles. The average size of the crystals was estimated using the Scherrer equation. The decomposition temperature of the reactants, their mixture, and the formation temperature of $LiMn_2O_4$ was examined by TGA, thermal gravimetric analysis (Rheometric scientific model). Also, the appropriate temperature for the calcination of the particles was determined by TGA. All TGA tests were conducted at a temperature ramp of 10°C/min. Dynamic light scattering device (HORIBA SZ-100 model) was also applied to study the average particle diameter. Although SEM images were not obtained in the current work, future studies will include SEM and TEM analysis for direct visualization of morphology and microstructural features.

Results

Examine the operating conditions of the reactor

Table **11** shows the temperature and flame height in different ratios of airflow to fuel flow. As can be seen, the flame length is an inverse function of the air-to-fuel ratio, and the flame length decreases as this ratio increases. While with the rise of air-to-fuel ratio, the flame temperature first has an upward trend and a downward one.

Thermal decomposition of reactants and the reaction mechanism

Thermal processes for the production of $LiMn_2O_4$ particles in a spray flame reactor consist of three stages [33, 34]:

A. Loss of crystallization water
B. Decomposition of reactants into metal oxides
C. The reaction between metal oxides

To determine the mechanism of $LiMn_2O_4$ synthesis and identify the thermal decomposition reactions in the spray flame reactor, the thermal decomposition of pure reactants and a stoichiometric liquid mixture, with a molar ratio of lithium to manganese equal to 0.5, were studied by TGA. Figure and Figure show the TGA results for pure reactants and the stoichiometric mixture, respectively.

Eqs 1 to 4 show the product formation mechanism in the flame process according to the results of Figure 4.

$$Mn(NO_3)_2 \cdot 4H_2O \rightarrow Mn(NO_3)_2 + 4H_2O \quad (1)$$

$$4Mn(NO_3)_2 \rightarrow 2Mn_2O_7 + 8NO + O_2 \quad (2)$$

$$Mn_2O_7 \rightarrow Mn_2O_3 + 2O_2 \quad (3)$$

$$2Mn_2O_3 \rightarrow 4MnO + O_2 \quad (4)$$

Figure shows that the $Mn(NO_3)_2.4H_2O$ at 120°C loses 30% of its mass due to water evaporation (Eq 1). Then, with increasing temperature from 120°C to about 180°C, the mass decreases with a steep slope of 55%, related to the formation of Mn_2O_7 (Eq 2). More mass reduction can be observed by increasing the temperature. At a temperature of nearly 230°C it reaches 30% of its initial mass, which is related to the formation of Mn_2O_3 (Eq 3). From 230°C to about 500°C, the mass of the substance does not change. At a temperature of about 500°C, the mass of the material decreases with a gentle slope. Finally, it reaches 28% of its initial value related to MnO formation (Eq 4). With the increasing temperature up to 900°C, no change in the mass of the material is observed. Also, according to this figure, the thermal decomposition process of $LiNO_3$, given by Eq 5, begins at 600°C and ends at 700°C with conversion to Li_2O (20% by mass).

$$4LiNO_3 \rightarrow 2Li_2O + 4NO_2 + O_2 \quad (5)$$

Figure shows $LiMn_2O_4$ is formed at about 480°C, begins to decompose at about 800°C, and converts to manganese oxides at 850°C, given by Eq 6. Similar results have been reported by Saadatkhah et al. [33] and Berbenni et al. [35].

$$3LiMn_2O_4 \rightarrow Mn_3O_4 + 3LiMnO_2 + O_2 \quad (6)$$

Considering the temperature range of the flame in the studied reactor and the temperature range of $LiMn_2O_4$ formation, Figure , it can be concluded that the formation of $LiMn_2O_4$ takes place according to Eq 7:

$$8MnO + 2Li_2O + 3O_2 \rightarrow 4LiMn_2O4 \quad (7)$$

Comparing Figure and 5 shows that the decomposition temperature of $LiNO_3$ in the mixture of reactants is about 220°C lower than the decomposition temperature in pure form. As Zhang et al. [3] mentioned, the reason for this could be the catalytic traits of manganese oxides produced in pyrolysis reactions.

Yield

Yield is defined as the mass ratio of the filtrate to the mass of the product expected from Eq 8.

$$2LiNO_3 + 4Mn(NO_3)_2 \rightarrow 2LiMn_2O_4 + 2NO_2 + 8NO + 5O_2 \quad (8)$$

All experiments were performed in 45 minutes, and the results are presented in Table **12**. The reasons for low yield can be particles sticking to the reactor wall, incomplete reactions, and side reactions. It should be noted that the collected product is not pure, and it is necessary to consider the results of X-ray diffraction tests before analyzing the given data in this table. Additional researches are required to identify and measure loss mechanisms, such as wall deposition and gas-phase nucleation, which can result in filter bypass. Potential advancements could involve refining reactor geometry, enhancing the efficiency of cyclone separators, and adjusting the flame configuration to minimize particle loss.

Crystal structure of particles

In addition to the mean particle size, the size distribution was analyzed using DLS. Broader distributions were observed at lower reactant concentrations, indicating less uniform nucleation. Narrower distributions correlated with higher crystallinity, supporting the influence of flame temperature and residence time. Uneven particle size can lead to irregular electrochemical behavior in batteries and will be addressed in future work.

Figure shows XRD results of produced particles from a 2M reaction solution with different air-to-fuel ratios. The figure shows the samples have a crystalline structure, and the position of the peaks in samples 1 (ratio 12.5) and 6 (ratio 9.5) correspond to the standard sample, which indicates the crystal formation of the material ($LiMn_2O_4$). Nevertheless, in sample 1, there is evidence for impurities related to the formation of the crystalline phase of Mn_2O_3. In sample 6, LMO crystalline phases are consistent with the main spinel peaks of $LiMn_2O_4$ (plates (111), (311) and (400)) and the space group Fd3m, which indicates the formation of the LMO phase and the absence of impurities. Sample 7 (the ratio of 6.5) and the standard sample are compatible only at an angle of 18.6°, and Mn_2O_3 is the significant product, leading to the disappearance of $LiMn_2O_4$ crystal. According to Table **12**, experiment 8, in the air-to-fuel ratio of 6.5 and a 1.1M reactant solution, has the highest yield. In contrast, in the same concentration of reactant solution, the lowest efficiency is related to experiment (9) with a ratio of 12.5. For the 2M solution, the highest and lowest yields belong to the ratio of 6.5 and 9.5, respectively. However, the difference in yield for the ratio of 12.5 is not much different from the ratio of 9.5. This trend can be explained by the flame temperature and the residence time of the particles. At a ratio of 12.5, due to the short flame height, in Table **11**, the production reactions of $LiMn_2O_4$ are not complete. However, at the ratio of 6.5, the reaction rate is expected to be slower than at other ratios due to lower flame temperature. Therefore, the possible chemical reactions are incomplete, and more by-products are produced. In Experiment 6, due to the high temperature of the flame (950°C) compared to the other two experiments, evaporation, decomposition, and chemical reactions have more chance to be complete. It results in to increase in the crystallinity of $LiMn_2O_4$. In Experiment 1, due to the lower fuel flow rate than in Experiment 6, the residence time of the particles inside the reactor is longer. In this case, further decomposition and oxidation reactions are possible, and particles with higher purity and crystallinity can be produced. However, due to the short flame length (8cm) and also the lower flame temperature (850°C) compared to experiment 6, despite the more extended residence, since the particles are exposed to flame for less time, the crystallinity of the product decreased compared to sample 6. The residence time of the particles inside the reactor is the shortest in experiment 7 due to the high fuel flow. However, the particles expose more to the flame due to the high flame height (20cm). Therefore, higher reaction progress and consequently purer

and more crystalline product is expected. However, the results indicate that the low flame temperature (620°C) overcame its long length and has resulted in incomplete reactions, despite the long residence time of the particles in the flame. In this case, $LiMn_2O_4$ crystals do not form. Another reason could be the inadequate oxygen for the oxidation reactions required to form $LiMn_2O_4$.

Figure shows XRD results for a 1.1M reactant solution. The figure shows that in samples 2 and 10 (air-to-fuel ratio 9.5), the crystallinity of $LiMn_2O_4$ particles has increased, and in sample 8 (ratio 6.5), $LiMn_2O_4$ spinel has not formed. Figure shows the effect of the air-to-fuel ratio on the formation of $LiMn_2O_4$ particles for a 0.2M reactant solution, where $LiMn_2O_4$ spinel has not formed except in sample 4 (ratio 9.5).

Overall, it can be concluded that high flame temperature completes the thermal reactions in the flame and leads to the formation of $LiMn_2O_4$ spinel and increase its crystallinity. In a low-temperature flame, reactions are incomplete or unwanted side reactions occur, leading to the no formation of a $LiMn_2O_4$ spinel.

Also, to determine the average particle size, produced particles were dispersed in distilled water by an ultrasonic mist, and a dynamic light scattering analyzer measured their diameter. The results of the mean particle diameter size, D_n, are given in Table 4. Sample 5 (concentration 0.2M and ratio 12.5) and sample 7 (concentration 2M and ratio 6.5) have the smallest and highest mean particle sizes.

Analysis of experiments by Response surface methodology (RSM)

The effect of influential factors on system responses (average particle size and yield) is investigated, and the proposed model and response Surface diagrams resulting from Design Expert software are analyzed. The results are shown in Table **13**. The F value of the model is 43.80, which shows that the model presented by Eq 9, with a correlation coefficient of 0.98, is significant and can well describe the system's behavior

$$Yield = 13.36 + 48.05\,B - 3.29\,A + 0.09\,AB - 18.96\,B^2 + 0.13\,A^2 \quad (9)$$

The value of F for lack of fit is 9.91, which indicates the appropriateness of the chosen model. Also, the results of central composite design variance for the average particle size produced are shown in Table **14**. Eq 10 shows the linear model provided by Design-Expert software for predicting and calculating the average particle size. The adequate precision (signal to noise ratio) is 18.5, and the correlation coefficient is 0.93, which indicates that the model can be used well in the study area.

$$Mean\ Size = 341.94 + 99.26\,B - 13.06\,A \quad (10)$$

Conclusion

This study demonstrates an innovative approach using a premixed flame-assisted spray pyrolysis reactor, allowing enhanced control over particle properties and potential scalability. Although this study focused on optimizing synthesis conditions and material characterization, future work will evaluate the electrochemical properties of the produced $LiMn_2O_4$ particles,

including capacity, cycling performance, and rate capability, to assess their suitability for battery applications. Lithium manganese oxide particles, $LiMn_2O_4$, were produced from an aqueous solution including metal salts $LiNO_3$ and $Mn(NO_3)_2{\cdot}4H_2O$ by a premixed flame-assisted spray pyrolysis reactor. According to TGA, Lithium manganese oxide is formed in the temperature range of 480°C to 800 °C and decomposes at 850°C. The significant impurity even after thermal decomposition is Mn_2O_3. $LiMn_2O_4$ crystals have a higher crystallinity at an air-to-fuel ratio of 9.5. A more concentrated reactant solution leads to a product with higher crystallinity. The highest purity of the $LiMn_2O_4$ crystalline phase occurs at an air-to-fuel ratio of 9.5 and a reactant solution concentration of 2M. As the flame length, reagent concentration and residence time increase, the average particle size in the final product increases. In general, the interactions between the two parameters of the air-to-fuel ratio, which controls the temperature and residence time of particles in the flame, and the concentration of the reactant solution, determine the crystallinity and final particle size. According to the analysis of variance achieved by Design-Expert software, the concentration of the reactant solution has the most significant effect on the average particle size and yield. A linear model describes the product's particle size with correlation coefficients of 0.9266, and a binomial model with correlation coefficients of 0.9821 describes the yield.

References

1. Hermawan A., Wibowo A., Asri L.A.T.W. et al. "Improved ionic conductivity of porous $Li_4Ti_5O_{12}$ synthesized by sol-gel method using eggshell membrane as soft template", *Mater Res Express*, **6**(7), pp. 075030, (2019), DOI:https://doi.org/10.1088/2053-1591/ab1298.
2. Saadatkhah N., Aghamiri S., Talaie M.R. et al. "Flame-assisted spray pyrolysis to size-controlled $Li_yAl_xMn_{2-x}O_4$: a supervised machine learning approach", *CrystEngComm*, **20**(46), pp. 7590-601, (2018), DOI:https://doi.org/10.1039/C8CE01026A.
3. Zhang X., Zheng H., Battaglia V. et al. "Electrochemical performance of spinel $LiMn_2O_4$ cathode materials made by flame-assisted spray technology", *J Power Sources*, **196**(7), pp. 3640-5, (2011), DOI:https://doi.org/10.1016/j.jpowsour.2010.07.008.
4. Zou H., Wang B., Wen F. et al. "Hydrothermal synthesis of pure $LiMn_2O_4$ from nanostructured MnO_2 precursors for aqueous hybrid supercapacitors", *Ionics*, **23**(5), pp. 1083-90, (2017), DOI:https://doi.org/10.1007/s11581-016-1927-3.
5. Zhang X. Aerosol synthesis of cathode materials for Li-ion batteries: Washington University in St. Louis; 2011.
6. Purwanto A., Yudha C.S., Muhammad K.I. et al. "Synthesis of $LiNi_{0.8}Co_{0.15}Al_{0.05}O_2$ cathode material via flame-assisted spray pyrolysis method", *Adv Powder Technol*, **31**(4), pp. 1674-81, (2020), DOI:https://doi.org/10.1016/j.apt.2020.01.035.
7. Li S., Ren Y., Biswas P. et al. "Flame aerosol synthesis of nanostructured materials and functional devices: Processing, modeling, and diagnostics", *Prog Energy Combust Sci*, **55**, pp. 1-59, (2016), DOI:https://doi.org/10.1016/j.pecs.2016.04.002.
8. Meierhofer F. and Fritsching U. "Synthesis of Metal Oxide Nanoparticles in Flame Sprays: Review on Process Technology, Modeling, and Diagnostics", *Energy Fuels*, **35**(7), pp. 5495-537, (2021), DOI:https://doi.org/10.1021/acs.energyfuels.0c04054.
9. Zang G., Zhang J., Xu S. et al. "Techno-economic analysis of cathode material production using flame-assisted spray pyrolysis", *Energy*, **218**, pp. 119504, (2021), DOI:https://doi.org/10.1016/j.energy.2020.119504.

10. Hirano T., Nakakura S., Rinaldi F.G. et al. "Synthesis of highly crystalline hexagonal cesium tungsten bronze nanoparticles by flame-assisted spray pyrolysis", *Adv Powder Technol*, **29**(10), pp. 2512-20, (2018), DOI:https://doi.org/10.1016/j.apt.2018.07.001.
11. Teoh W.Y. "Flame Synthesis of Simple and Multielemental Oxide Catalysts." In *Heterogeneous Catalysts*, Teoh W.Y., Urakawa A., Ng Y.H., Sit P., Ed. pp. 183-201, WILEY-VCH GmbH (2021), DOI:https://doi.org/10.1002/9783527813599.ch10.
12. Meierhofer F., Mädler L. and Fritsching U. "Nanoparticle evolution in flame spray pyrolysis—Process design via experimental and computational analysis", *AlChE J*, **66**(2), pp. e16885, (2020), DOI:https://doi.org/10.1002/aic.16885.
13. Strobel R. and Pratsinis S.E. "Flame aerosol synthesis of smart nanostructured materials", *J Mater Chem*, **17**(45), pp. 4743-56, (2007), DOI:https://doi.org/10.1039/B711652G.
14. Rudin T., Wegner K. and Pratsinis S.E. "Uniform nanoparticles by flame-assisted spray pyrolysis (FASP) of low cost precursors", *J Nanopart Res*, **13**(7), pp. 2715-25, (2011), DOI:https://doi.org/10.1007/s11051-010-0206-x.
15. Jung D.S., Ko Y.N., Kang Y.C. et al. "Recent progress in electrode materials produced by spray pyrolysis for next-generation lithium ion batteries", *Adv Powder Technol*, **25**(1), pp. 18-31, (2014), DOI:https://doi.org/10.1016/j.apt.2014.01.012.
16. Abram C., Mezhericher M., Beyrau F. et al. "Flame synthesis of nanophosphors using sub-micron aerosols", *Proceedings of the Combustion Institute*, **37**(1), pp. 1231-9, (2019), DOI:https://doi.org/10.1016/j.proci.2018.06.040.
17. Camenzind A., Caseri W.R. and Pratsinis S.E. "Flame-made nanoparticles for nanocomposites", *Nano Today*, **5**(1), pp. 48-65, (2010), DOI:https://doi.org/10.1016/j.nantod.2009.12.007.
18. Koirala R., Pratsinis S.E. and Baiker A. "Synthesis of catalytic materials in flames: opportunities and challenges", *Chem Soc Rev*, **45**(11), pp. 3053-68, (2016), DOI:https://doi.org/10.1039/c5cs00011d.
19. Zhao Z., Li Y., Chen Z. et al. "Value-added recycling of spent $LiFePO_4$ by a $FeCl_3$ leaching-spray pyrolysis approach", *J Power Sources*, **628**, pp. 235939, (2025), DOI:https://doi.org/10.1016/j.jpowsour.2024.235939.
20. Zhou Y., Li Y., Chen Z. et al. "Preferential lithium extraction and simultaneous ternary cathode precursor synthesis from spent lithium-Ion batteries using a spray pyrolysis-based process", *Sep Purif Technol*, **353**, pp. 128486, (2025), DOI:https://doi.org/10.1016/j.seppur.2024.128486.
21. Jang H., Seong C., Suh Y. et al. "Synthesis of lithium-cobalt oxide nanoparticles by flame spray pyrolysis", *Aerosol Sci Technol*, **38**(10), pp. 1027-32, (2004), DOI:https://doi.org/10.1080/027868290524016.
22. Ernst F.O., Kammler H.K., Roessler A. et al. "Electrochemically active flame-made nanosized spinels: $LiMn_2O_4$, $Li_4Ti_5O_{12}$ and $LiFe_5O_8$", *Mater Chem Phys*, **101**(2-3), pp. 372-8, (2007), DOI:https://doi.org/10.1016/j.matchemphys.2006.06.014.
23. Aromaa M., Keskinen H. and Mäkelä J.M. "The effect of process parameters on the Liquid Flame Spray generated titania nanoparticles", *Biomol Eng*, **24**(5), pp. 543-8, (2007), DOI:https://doi.org/10.1016/j.bioeng.2007.08.004.
24. Patey T.J., Büchel R., Nakayama M. et al. "Electrochemistry of $LiMn_2O_4$ nanoparticles made by flame spray pyrolysis", *Phys Chem Chem Phys*, **11**(19), pp. 3756-61, (2009), DOI:https://doi.org/10.1039/B821572N.

25. Yi J.H., Kim J.H., Koo H.Y. et al. "Nanosized $LiMn_2O_4$ powders prepared by flame spray pyrolysis from aqueous solution", *J Power Sources*, **196**(5), pp. 2858-62, (2011), DOI:https://doi.org/10.1016/j.jpowsour.2010.11.038.
26. Choi S.H., Kim J.H., Ko Y.N. et al. "Electrochemical properties of boron-doped $LiMn_2O_4$ nanoparticles covered with glass material prepared by high-temperature flame spray pyrolysis", *Int J Electrochem Sci*, **8**, pp. 1146-62, (2013), DOI:https://doi.org/10.1016/S1452-3981(23)14087-9.
27. Aboulouard A., Gultekin B., Can M. et al. "Dye sensitized solar cells based on titanium dioxide nanoparticles synthesized by flame spray pyrolysis and hydrothermal sol-gel methods: a comparative study on photovoltaic performances", *J Mater Res Technol*, **9**(2), pp. 1569-77, (2020), DOI:https://doi.org/10.1016/j.jmrt.2019.11.083.
28. Zhang J., Xu S., Hamad K.I. et al. "High retention rate NCA cathode powders from spray drying and flame assisted spray pyrolysis using glycerol as the solvent", *Powder Technol*, **363**, pp. 1-6, (2020), DOI:https://doi.org/10.1016/j.powtec.2019.12.057.
29. Madero J.E., Li J., Shen K.-Y. et al. "An approach to low-temperature flame spray pyrolysis for the synthesis of temperature-sensitive materials: Application to $Li_{1.2}Mn_{0.54}Ni_{0.13}Co_{0.13}O_2$", *ApplEnerg Combut Sci*, **5**, pp. 100020, (2021), DOI:https://doi.org/10.1016/j.jaecs.2020.100020.
30. Minegishi N., Li P., Nagasawa T. et al. "Effect of flame temperature on structure and CO oxidation properties of Pt/CeO_2 catalyst by flame-assisted spray pyrolysis", *ApplEnerg Combut Sci*, **20**, pp. 100303, (2024), DOI:https://doi.org/10.1016/j.jaecs.2024.100303.
31. Chen X., Zou G., Yuan Y. et al. "Flame spray pyrolysis synthesized Ni-doped Fe/Ce oxygen carriers for chemical looping dry reforming of methane", *Fuel*, **343**, pp. 127913, (2023), DOI:https://doi.org/10.1016/j.fuel.2023.127913.
32. Li C., Lei J., Gu X. et al. "Preparation of $Bi_4Ti_3O_{12}/TiO_2$ by flame spray pyrolysis for photoelectrocatalytic degradation of tetracycline", *J Cleaner Prod*, **460**, pp. 142557, (2024), DOI:https://doi.org/10.1016/j.jclepro.2024.142557.
33. Saadatkhah N., Aghamiri S., Talaie M.R. et al. "Flame-assisted spray pyrolysis of lithium and manganese precursors to polycrystalline $LiMn_2O_4$", *Can J Chem Eng*, **97**(8), pp. 2299-308, (2019), DOI:https://doi.org/10.1002/cjce.23302.
34. Wu W., Wang K., Li Y. et al. "Nanocrystalline $LiMn_2O_4$ preparation and kinetics of thermal process of precursor", *J Therm Anal Calorim*, **112**(3), pp. 1391-9, (2013), DOI:https://doi.org/10.1007/s10973-012-2740-5.
35. Berbenni V. and Marini A. "Thermoanalytical (TGA-DSC) and high temperature X-ray diffraction (HT-XRD) study of the thermal decomposition processes in Li_2CO_3–MnO mixtures", *J Anal Appl Pyrolysis*, **64**(1), pp. 43-58, (2002), DOI:https://doi.org/10.1016/S0165-2370(01)00169-3.

Figure 1: Schematic of flame-assisted spray pyrolysis reactor setup

1- Ultrasonic spraying system, 2-Quartz cylindrical reactor with a length of 600mm and a diameter of 80mm, 3-Torch with triple inlet, 4-Product collection system including filter, 5-Fuel (city gas), 6 -Carrier gas (air), 7-Oxidizing agent (air)

Figure 2: Schematic of reactant solution spray system

1-Ultrasonic misting, 2- Carrier gas (air), 3- Spray nozzle with an inner diameter of 4 mm and an outer diameter of 20 mm

Figure 3: Schematic of the particle collection system

1-Gas flow inlet, 2- Metal filter with a diameter of 60 nm, 3- Fiberglass filter with a diameter of 60 nm, 4- Filter holder with an inner diameter of 60 nm and an outer diameter of 100 nm, 5- Gas flow output

Figure 4: TGA diagrams for pure $LiNO_3$ and $Mn(NO_3)_2.4H_2O$ Figure 5: TGA diagram of the stoichiometric mixture of $LiNO_3$ and $Mn(NO_3)_2.4H_2O$

Figure 6: Diffraction pattern of samples in different ratios of air to fuel at a concentration of 2M

Figure 7: Diffraction pattern of samples in different ratios of air-to-fuel at a concentration of 1.1 M

Figure 8: Scattering pattern of samples in different ratios of air-to-fuel at a concentration of 0.2 M

Table 1: City gas Composition

Table 2: Levels and variables selected for experiment design

Table 3: Experimental design recommended by the response surface methodology

Table 4: Flame temperature and height for different ratios of airflow to fuel flow

Table 5: Product production efficiency for the tests in Table 2

Table 6: Results of variance test for yield

Table 7: Results of variance test for average particle size

Table 8: City gas Composition

Component	Concentration	Unit
H_2S	<1	ppm
N_2	3.8	
C1	90.0	
CO_2	0.6	
C2	4.0	
C3	1.06	
iC4	0.17	
nC4	0.24	mol%
iC5	0.06	
nC5	0.04	
C6	0.02	
C7	0.01	
Total	100	

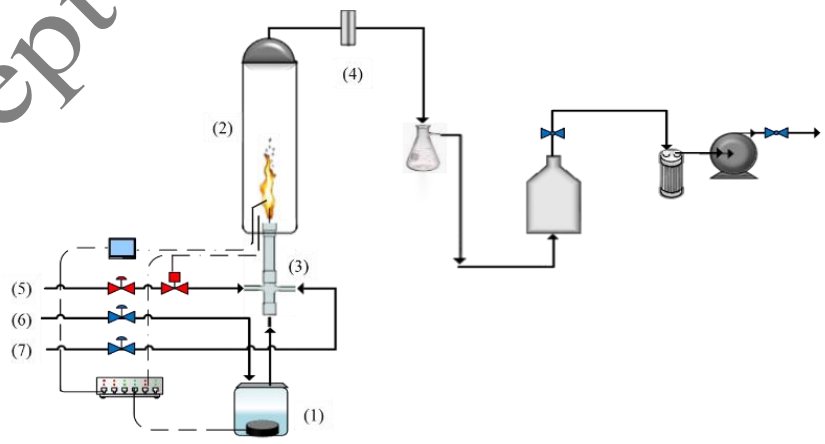

Figure 1: Schematic of flame-assisted spray pyrolysis reactor setup

1- Ultrasonic spraying system, 2-Quartz cylindrical reactor with a length of 600mm and a diameter of 80mm, 3-Torch with triple inlet, 4-Product collection system including filter, 5-Fuel (city gas), 6 -Carrier gas (air), 7-Oxidizing agent (air)

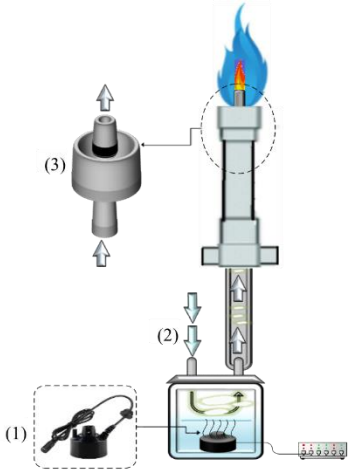

Figure 2: Schematic of reactant solution spray system
1-Ultrasonic misting, 2- Carrier gas (air), 3- Spray nozzle with an inner diameter of 4 mm and an outer diameter of 20 mm

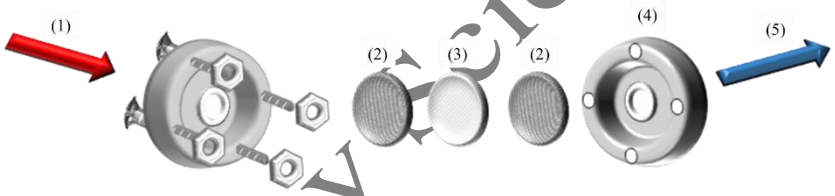

Figure 3: Schematic of the particle collection system
1-Gas flow inlet, 2- Metal filter with a diameter of 60 nm, 3- Fiberglass filter with a diameter of 60 nm, 4- Filter holder with an inner diameter of 60 nm and an outer diameter of 100 nm, 5- Gas flow output

Table 9: Levels and variables selected for experiment design

Variables	levels		
	-1	0	+1
Concentration of the reactant solution (M)	0.2	1.1	2
Air flow rate to fuel flow rate ratios (vol/vol)	6.5	9.5	12.5

Table 10: Experimental design recommended by the response surface methodology

Experiments	Air flow rate to fuel flow rate ratios (vol/vol)	Concentration of the reactant solution (M)
1	12.5	2
2	9.5	1.1
3	6.5	0.2
4	9.5	0.2
5	12.5	0.2

6	9.5	2
7	6.5	2
8	6.5	1.1
9	12.5	1.1
10	9.5	1.1

Table 11: Flame temperature and height for different ratios of airflow to fuel flow

Air flow rate to fuel flow rate ratios (vol/vol)	Flame length (cm)	Flame temperature (°C)
6.5	20	620
9.5	12	950
12.5	8	850

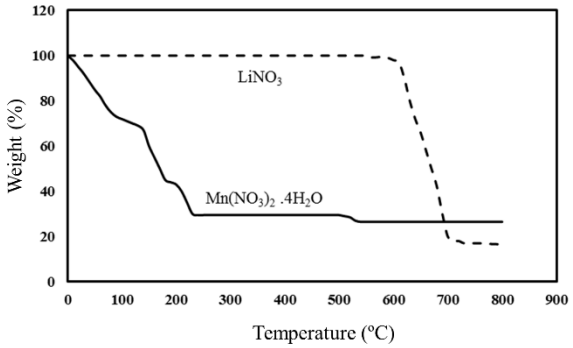

Figure 4: TGA diagrams for pure $LiNO_3$ and $Mn(NO_3)_2.4H_2O$

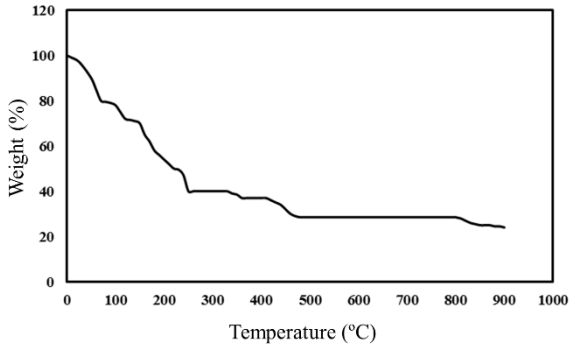

Figure 5: TGA diagram of the stoichiometric mixture of $LiNO_3$ and $Mn(NO_3)_2.4H_2O$

Table 12: Product production efficiency for the tests in Table 2

Experiments	Air flow rate to fuel flow rate ratios (vol/vol)	Concentration (M)	Yield (%)	Average particle size* (nm) $D_n = \frac{\sum n_i d_i}{\sum n_i}$
1	12.5	2	16	370
2	9.5	1.1	24	362
3	6.5	0.2	5	257

4	9.5	0.2	3	216
5	12.5	0.2	2	210
6	9.5	2	15	413
7	6.5	2	18	436
8	6.5	1.1	30	386
9	12.5	1.1	21	264
10	9.5	1.1	25	357

* n_i represents the number of particles in diameter d_i

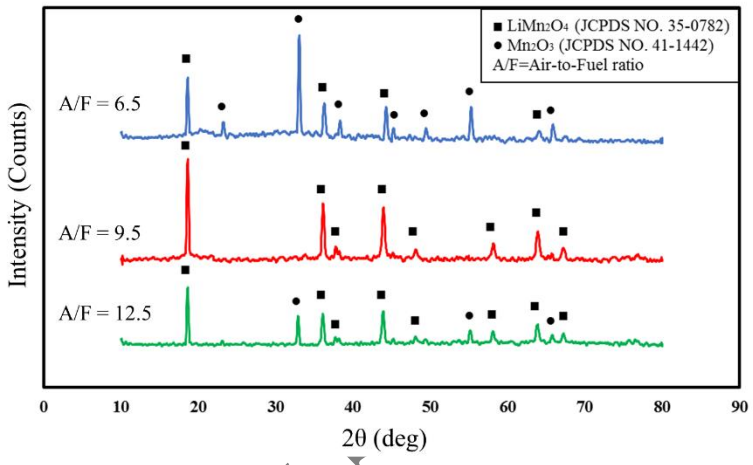

Figure 6: Diffraction pattern of samples in different ratios of air to fuel at a concentration of 2M

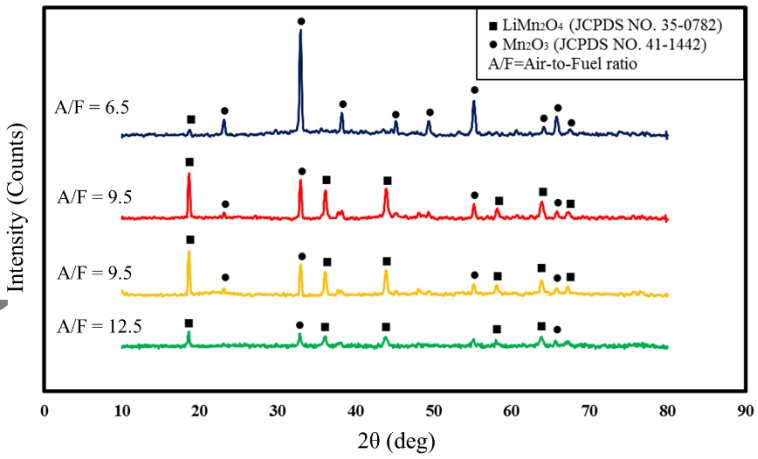

Figure 7: Diffraction pattern of samples in different ratios of air-to-fuel at a concentration of 1.1 M

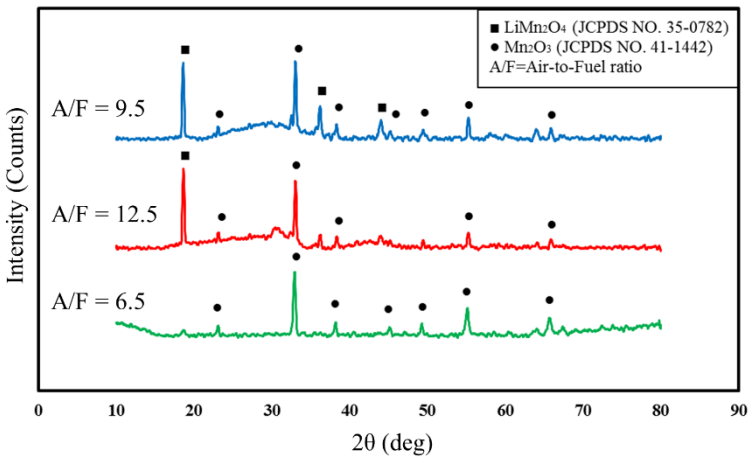

Figure 8: Scattering pattern of samples in different ratios of air-to-fuel at a concentration of 0.2 M

Table 13: Results of variance test for yield

Source	Sum of squares	df	Mean square	F-value	P-value	
Model	481.53	5	168.31	43.80	0.0014	Significant
A*	253.50	1	253.50	65.98	0.0012	
B**	32.67	1	32.67	8.50	0.0434	
AB	0.25	1	0.25	0.065	0.8112	
A^2	550.30	1	550.30	143.22	0.0003	
B^2	3.05	1	3.05	0.79	0.4235	
Residual	15.37	4	3.84			
Lack of Fit	14.87	3	4.96	9.91	0.2284	Not Significant
Pure Error	0.5	1	0.50			

* concentration of the reactant solution (M)

** air-to-fuel ratio (vol/vol)

Table 14: Results of variance test for average particle size

Source	Sum of squares	df	Mean square	F-value	P-value	
Model	57086.8	2	28543.4	44.16	0.0001	Significant
A*	47882.6	1	47882.6	74.09	<0.0001	
B**	9204.1	1	9204.1	14.24	0.0069	
Residual	4224.0	7	646.3			
Lack of Fit	4511.5	6	751.9	60.15	0.0984	Not Significant
Pure Error	12.50	1	12.50			

* concentration of the reactant solution (M)

** air-to-fuel ratio (vol/vol)

Hamid Iravani, has Master's degree in Chemical Engineering from University of Isfahan in 2019. His academic and professional focus is on the synthesis and characterization of nanomaterials, with a particular emphasis on materials for energy storage technologies, especially lithium-ion

batteries. Throughout his studies and professional activities, He has participated in numerous research projects aimed at developing nanomaterials with improved electrochemical performance and greater stability. His areas of interest also include environmentally-friendly synthesis methods and scalable production technologies for industrial applications. Currently, he works as a chemical engineer at Isfahan Petrochemical Company, where he contribute to process optimization and the integration of advanced materials into chemical production lines. His interdisciplinary expertise bridges the gap between nanotechnology research and its practical applications in the energy and chemical industries. He is always seeking opportunities for innovation and collaboration in the fields of nanomaterials, sustainable energy, and advanced chemical engineering.

Mohammad Hojat is an Assistant Professor in the Department of Chemical Engineering at the University of Isfahan. He earned his BSc and MSc degrees in Chemical Engineering from Sharif University of Technology and completed his PhD in Chemical Engineering at Isfahan University of Technology. From 2020 to 2025, he was recognized as one of the top 2% most-cited scientists of the world for five consecutive years. His research focuses on the hydrodynamics and heat transfer of nanofluids, advanced gas adsorption systems and carbon capture technologies, and the application of artificial intelligence in chemical engineering.

Dr. Mohsen Gholami is a postdoctoral researcher at the Vrije Universiteit Brussel (VUB), affiliated with the Chemical Engineering department. His research focuses on advanced gas adsorption processes and carbon capture technologies, particularly through the development of hybrid adsorbents and electrified desorption techniques. Dr. Gholami has contributed to innovations such as induction heating methods for thermal swing adsorption and has co-authored numerous peer-reviewed publications in high-impact journals. Actively engaged in the STEPChem research group at VUB, he collaborates with experts to advance sustainable chemical processes. Prior to joining VUB, Dr. Gholami was an assistant professor at the University of Isfahan, where he supervised multiple master's theses on gas adsorption and carbon capture. His academic journey includes a Ph.D. in Chemical Engineering, and his expertise spans gas adsorption, CO_2 capture, and process intensification strategies.

Dr Mohammad Reza Talaei was formerly a professor in the Chemical Engineering Department at Shiraz University, Shiraz, Iran. He has been performing research in the environmental engineering field, including air, water, and soil pollution remediation. He is working as a researcher at the University of Calgary, Calgary, Canada, conducting research on Stormwater Management. He has published more than 100 scientific articles in the field.

SeyedFoad Aghamiri is an Emeritus Professor at University of Isfahan, Iran, and currently serves as an Adjunct Professor at the International Business University, Canada. He also holds the position of System Performance Analyst at eStorage, where he focuses on the performance optimization of energy storage systems. His research interests span climate change, energy systems, materials science, modeling, and data analytics. With decades of academic and industrial experience, Professor Aghamiri has contributed extensively to interdisciplinary approaches in energy and environmental sustainability, integrating advanced modeling techniques and data-driven analysis to address complex global challenges.